Hindawi

Research Article

Seismic Behavior Investigations of the Haunched Joint with Ribbed Anchor Webs in CFDST Structures

Yufen Zhang [iD],[1,2] Xiaokun Qu,[1] Ling Wang [iD],[1,2] Hongfan Bu,[1] and Shengxi Cao[3]

[1]*School of Civil and Transportation Engineering, Hebei University of Technology, Tianjin, China*
[2]*Tianjin Key Laboratory of Prefabricated Buildings and Intelligent Constructing, Hebei University of Technology, Tianjin, China*
[3]*Norendar International Ltd., Shijiazhuang 050011, China*

Correspondence should be addressed to Ling Wang; wlark@sina.com

The haunched joint with ribbed anchor webs in the concrete-filled double steel tubular (CFDST) structure was proposed in this study. The CFDST column and the steel beam were connected by ribbed webs, which were anchored inside the column and connected to the beam web by the bolted connection, and haunches were welded to shift plastic hinges from the joint core to the beam end. The cyclic loading test was conducted on three beam-to-column joint specimens. Seismic behaviors, including failure modes, strain and stress responses, hysteretic curves, ductility, and energy dissipation capacity, were, respectively, analyzed. Besides, finite element (FE) modeling was validated and was used to further analyze the seismic behavior in consideration of connection constructional details, geometric dimensions, material strength, and axial compression ratios. The parametric investigation shows that besides ribs and haunches, stiffening diaphragms are practicable to connect the double tubes, especially for the high-strength steel beam; beam-to-column bending stiffness ratio per unit length is appropriate to be 0.3–0.5; choosing low strength grade of concrete is allowed to satisfy engineering requirements; the axial compression ratio should be limited within 0.5.

1. Introduction

The concrete-filled double steel tubular (CFDST) column, composed of the circular section, offers improved axial strength, ductility, and energy absorptions compared to its CFST counterparts and, therefore, has significant potential to be widely applied in future constructions, especially in high-intensity earthquake areas [1–4]. Besides, CFDST column facilitates the selection of eco-friendly and green concrete, reducing the adverse impact of concrete on the environment [5]. Another advantage of the CFDST column is that when it is composed of an outer square tube and an inner round tube, it is easy to connect with H-shaped steel beams [6, 7]. As far as the connections were concerned, many studies on the performance of connections between square CFST columns and steel beams under static and quasistatic loading have been carried out during the past decades [8]. Among the research achievements, the vertical stiffener joint and the external diaphragm joint have been applied in the CFDST structure [9, 10]. However, the double steel tubes in one

CFDST column haven't taken functions in the connection to steel beams. For example, blind bolts were anchored inside the inner tube and a strong anchoring function was guaranteed for force transmission of the joint [11]. So, the anchor webs welded between the double tubes would also play a better role in force transfer to reinforce the beam-to-CFDST column connection. Wang et al. [12] tested existing reinforced concrete columns enhanced by web indirect bonding and web direct bonding combined with a steel end plate, and Luo and Wu [13] applied steel plate–concrete joints to strengthen the engineering structures, in which the steel plates and concrete were connected with anchors. The research results showed that the ultimate loads of the specimens using anchor steel plates improved a lot. Hu et al. [14] studied the mechanical performance of the prefabricated concrete beam with H-shaped steel joints and found that when the section was the same, the deformation of the member connected only with webs was greater than that of the member connected with flanges and webs. Therefore, a rib stiffener beam connection was designed between a CFST
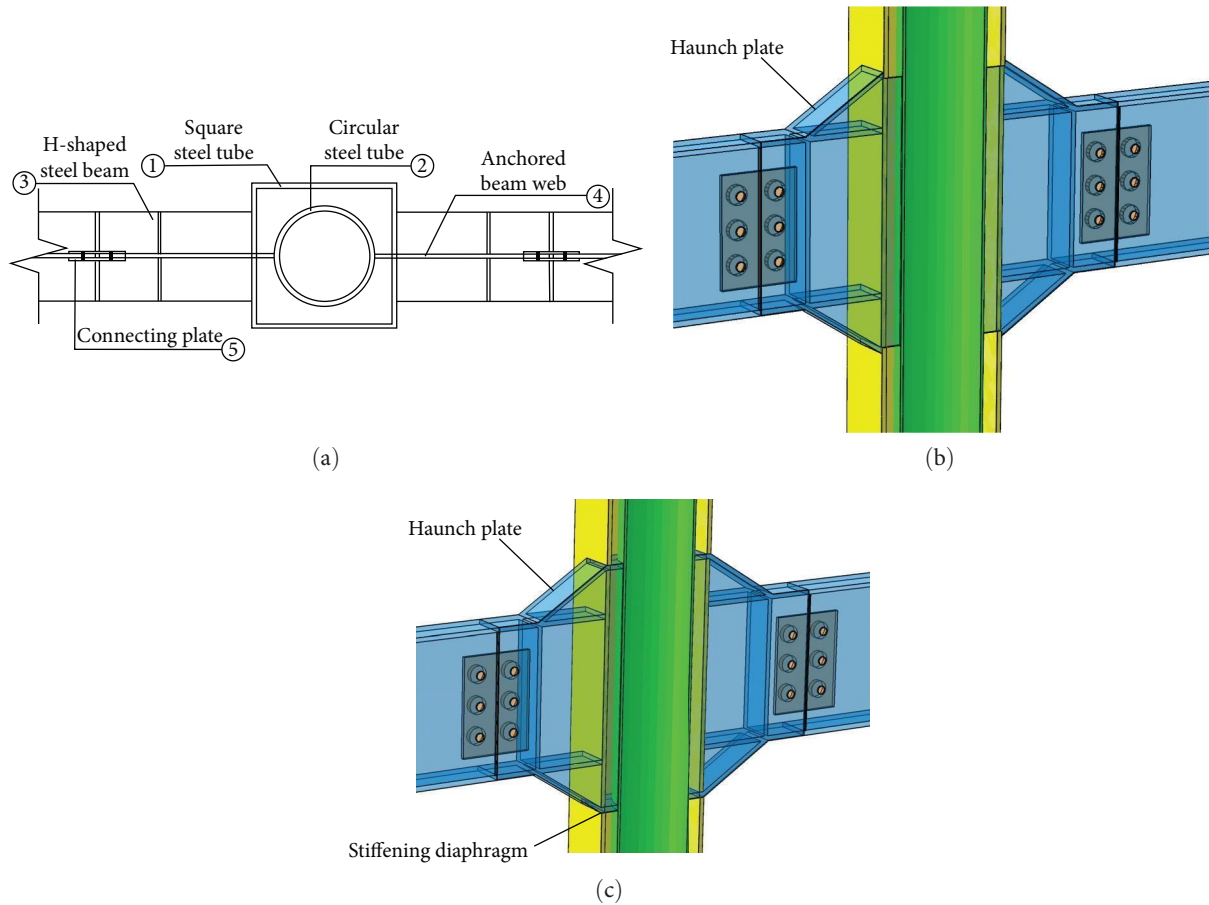
(a)

(b)

(c)

FIGURE 1: Construction of specimens. (a) Plan view. (b) Cutaway view of SPJ1 and SPJ2. (c) Cutaway view of SPJ3.

column and an I-beam [15], and a rib stiffener similar to a vertical through-web was proposed to improve the connection's rigidity and ductility.

To avoid a sudden collapse of beam-to-column connections during earthquakes, installing haunches is a useful constructional measure in seismic designs because it can enhance joint stiffness and prevent plastic failure from columns [16–20]. A cyclic loading test on the steel moment-resisting connection with straight haunches was carried out by Lee et al. [21], and the strut effect of haunches was verified. Van-Long et al. [22] employed T-shaped hammerheads to simplify the haunch fabrication, and this method conformed to the plastic design requirements specified in EN 1993-1-8 [23]. Meanwhile, welding haunches have been proved to be an economical constructional measure in beam-to-column joints to achieve essential mechanical performances [24–26]. Chu et al. [27] and Dong et al. [28], respectively, investigated seismic behaviors of the steel beam-to-CFDST column joint and the steel joint stiffened by haunches, and the results showed that the installation of haunches improved energy dissipation capacity and ductility.

Combining the advantages of vertically ribbed webs and haunches, haunched joints with ribbed anchor webs were designed as rigid joints in CFDST structures in this study. Three joint specimens were manufactured for cyclic loading

tests, and failure modes, ultimate bearing capacity, initial stiffness, ductility, and other indexes were analyzed. Afterward, a series of finite element (FE) models was established, and the obtained FE analysis results were verified by comparing them with test results; then, parametric analyses on seismic behaviors were conducted based on FE models.
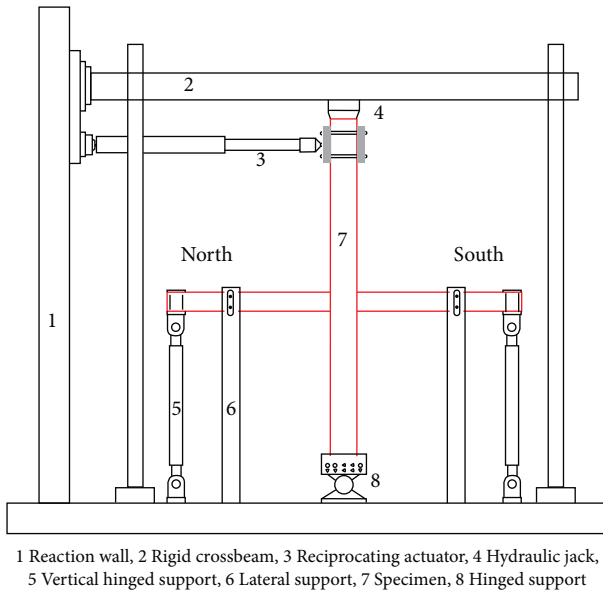
2. Test Overview

2.1. Design of Specimens. Following the design criterion of "strong column and weak beam," cross-sectional dimensions of the inner and the outer steel tubes were designed as 194 mm × 6 mm and 280 mm × 10 mm, respectively, as shown in the plan of the joint (Figure 1(a)). Vertically ribbed webs were welded on the circular steel tube and connected to beam webs using bolted connections, and then haunch plates were set to form the haunched joint, as shown in the cutaway views (Figures 1(b) and 1(c)). For the steel beams, two cross-sectional dimensions were selected to study the influence of cross-sectional dimensions on the seismic behaviors of the joint. One was H346 mm × 174 mm × 6 mm × 9 mm for specimen SPJ1, and the other was H350 mm × 175 mm × 7 mm × 11 mm for specimens SPJ2 and SPJ3. As for specimen SPJ3, as shown in Figure 1(c), stiffening diaphragms were set between the two tubes to investigate differences in the force transfer path based

TABLE 1: Parameters of each joint specimen.

Specimen no.	Anchor components	Dimensions of the steel beam (mm)
SPJ1	Vertically ribbed webs	H346×174×6×9
SPJ2	Vertically ribbed webs	H350×175×7×11
SPJ3	Vertically ribbed webs and stiffening diaphragms	H350×175×7×11

TABLE 2: Material properties.

Materials	Yield strength (MPa)	Ultimate strength (MPa)	Young's modulus (MPa)
Square steel tubes	337.90	460.38	2.13×10^5
Circular steel tubes	343.88	443.45	2.11×10^5
Vertically ribbed webs	284.51	400.79	1.98×10^5
Haunch plates	295.51	406.89	2.13×10^5
Beams H346×174×6×9	288.69	405.41	2.00×10^5
Beams H350×175×7×11	327.64	465.01	2.17×10^5
Concrete	–	60.80	3.61×10^4

1 Reaction wall, 2 Rigid crossbeam, 3 Reciprocating actuator, 4 Hydraulic jack,
5 Vertical hinged support, 6 Lateral support, 7 Specimen, 8 Hinged support

(a)   (b)

FIGURE 2: Test apparatuses. (a) Loading diagram. (b) Test site.

on that in specimen SPJ2. The CFDST column was 2,070 mm high, and the joint specimen was 3,700 mm long. The main design parameters of each joint specimen are shown in Table 1. In the process of making the specimen, there was a rectangular hole cut in the square steel tube at the beam-to-column connection in order to weld the anchorage web and stiffening diaphragm on the inner tubes, and then the hole was filled by plug welding. Last, concrete in the column was poured in vertical layers, and fine aggregate concrete was used. The concrete was vibrated and mixed continuously to ensure its compactness around the anchorage web and stiffening diaphragm.

2.2. Material Properties. The tensile coupon test for steel components was carried out in light of requirements in GB/T 228.1-2010 [29]. The uniaxial compressive strength of concrete cubic samples was 60 MPa. The actual material properties are shown in Table 2, where the average value of three test samples was taken as the measured value.

2.3. Test Apparatuses and the Loading Scheme. Test apparatuses are shown in Figure 2. The column bottom was fixed on the foundation by the hinged support, and the vertical hinged support was installed at beam ends to ensure free rotation and horizontal displacement of the beams in a specified plane. The lateral bracing was placed in case of torsion and overturn of the beam. The axial static load (N) was applied to the top of the column using a hydraulic jack, which remains vertical and reciprocates with the column top. The axial compression ratio in the test was determined to be 0.275, which was written as $n = N/N_u$, and N_u represented the ultimate axial bearing capacity of the CFDST column [30]. Lateral cyclic loads were applied to the top of the CFDST column by a
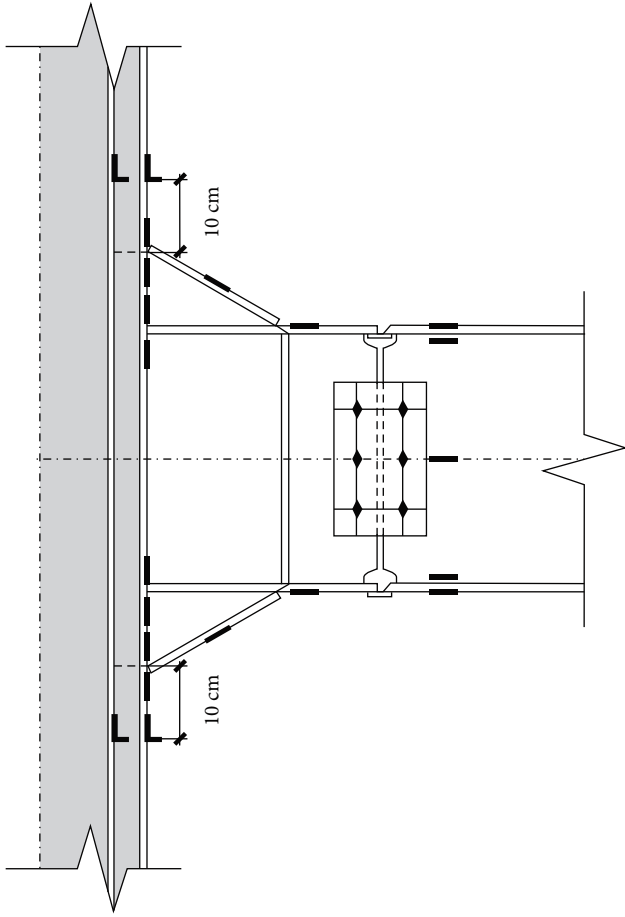
FIGURE 3: Layout of strain gauges.

horizontal actuator. During the loading process, a whole loading cycle was southward pushed first, then unloaded to the original point, and northward pulled again, finally unloaded. The southward push was regarded as the positive direction, and the northward pull was reversed.

The lateral cyclic loads were determined by the force and displacements in turn. For the early loading, namely, the elastic stage, the lateral force was 30 kN as one load grade, and it gradually increased until the lateral displacement of the column top reached the estimated yield displacement. The load step with the same displacement amplitude cycled twice until specimens were destroyed or the measured force decreased to less than 80% of the peak force. The point of failure was identified where the collapse force descended to 85% of the peak load. The layout of measuring points for the three joint specimens was the same. Figure 3 shows the layout of uniaxial strain gauges for measuring strains of steel components where probable large deformations appeared.

3. Finite Element Models

FE modeling with the same test conditions was conducted via ABAQUS program, so as to further analyze the influence of different parameters on seismic behaviors of the connection. The constitutive relation of materials, boundary conditions,

and interactions between different components were reasonably modeled, and corresponding details were elaborated as follows.

3.1. Constitutive Relation of Steel. The combined isotropic–kinematic hardening plastic behavior was selected to model the constitutive relation of steel components. The Poisson's ratio was 0.27 in line with the tensile coupon tests. Abdel-Rahman and Sivakumaran [31] evaluated the constitutive relations at the flat area and the corner area of channel steel, and the constitutive model proposed in that investigation was adopted for the square steel tube. Meanwhile, the constitutive model of the circular steel tube was established based on that of the flat area. Steel tube constitutive relation is given by Equations (1) and (2), respectively.

$$\sigma = \begin{cases} E_s\varepsilon & (\varepsilon \leq \varepsilon_e) \\ f_p + E_{s1}(\varepsilon - \varepsilon_e) & (\varepsilon_e < \varepsilon \leq \varepsilon_{e1}) \\ f_{ym} + E_{s2}(\varepsilon - \varepsilon_{e1}) & (\varepsilon_{e1} < \varepsilon \leq \varepsilon_{e2}) \\ f_y + E_{s3}(\varepsilon - \varepsilon_{e2}) & (\varepsilon_{e2} < \varepsilon \leq \varepsilon_{e3}) \end{cases}, \quad (1)$$

$$f_{y1} = f_y\left[0.6\frac{B_c}{(r/t)^m} + 0.4\right], \quad (2)$$

where f_y and f_u are the yield strength and tensile strength of the steel tube; f_p, f_{ym}, ε_{e1}, ε_{e2}, B_c, and m are given by Equations (3)–(8), respectively.

$$f_p = 0.75f_y, \quad (3)$$

$$f_{ym} = 0.875f_y, \quad (4)$$

$$\varepsilon_{e1} = \varepsilon_e + 0.125\frac{f_y}{E_{s1}}, \quad (5)$$

$$\varepsilon_{e2} = \varepsilon_{e1} + 0.125\frac{f_y}{E_{s2}}, \quad (6)$$

$$B_c = 3.69\frac{f_u}{f_y} - 0.819\left(\frac{f_u}{f_y}\right)^2 - 1.79, \quad (7)$$

$$m = 0.192\frac{f_u}{f_y} - 0.068. \quad (8)$$

The constitutive relations of the H-shaped steel beams, haunches, ribbed anchor webs, connecting plates, bolts, and stiffening diaphragms were simplified to trilinear models based on the tensile coupon tests.

3.2. Constitutive Relation of Concrete. The concrete damaged plasticity model [32] was adopted to simulate the mechanical behavior of concrete. Young's modulus was derived from the material property tests, and Poisson's ratio was 0.2. The tensile constitutive relation of the concrete referred to GB/T 50010-2010 [33]. In the test, the filled concrete in the column

was subjected to three-dimensional compression due to the confinement from the steel tube, so a confinement effect factor ξ [34] was introduced to compute the compressive stress–strain relation of concrete. The concrete between the square steel tube and the circular steel tube was calculated using the constitutive relation of the concrete filled with square steel tubes, and the concrete inside the circular steel tube was calculated using the constitutive relation of the concrete filled with circular steel tubes. Concrete compressive constitutive relation is given by Equation (9).

$$y = \begin{cases} \dfrac{2x - x^2}{x} & (x \le 1) \\ \dfrac{x}{\beta(x-1)^\eta + x} & (x > 1) \end{cases}, \tag{9}$$

where x and y are given by Equations (10) and (11), respectively.

$$x = \frac{\varepsilon}{\varepsilon_{c0}}, \tag{10}$$

$$y = \frac{\sigma}{\sigma_{c0}}, \tag{11}$$

$$\sigma_{c0} = f_c', \tag{12}$$

where f_c' is the compressive strength of concrete cylinder. Where ε_{c0}, η, and β are given by Equation (13)–(15), respectively.

$$\varepsilon_{c0} = \varepsilon_c + 800 \times \xi^{0.2} \times 10^{-6} \quad \left(\varepsilon_c = \left(1300 + 12.5 f_c'\right) \times 10^{-6}\right), \tag{13}$$

$$\eta = \begin{cases} (2.36 \times 10^{-5})^{[0.25 + (\xi - 0.5)^7]} \times f_c'^{0.5} \times 0.5 \ge 1.2 & \text{(concrete filled with circular steel tubes)} \\ \dfrac{f_c'^{0.1}}{1.2\sqrt{1+\xi}} & \text{(concrete filled with square steel tubes)} \end{cases}. \tag{15}$$
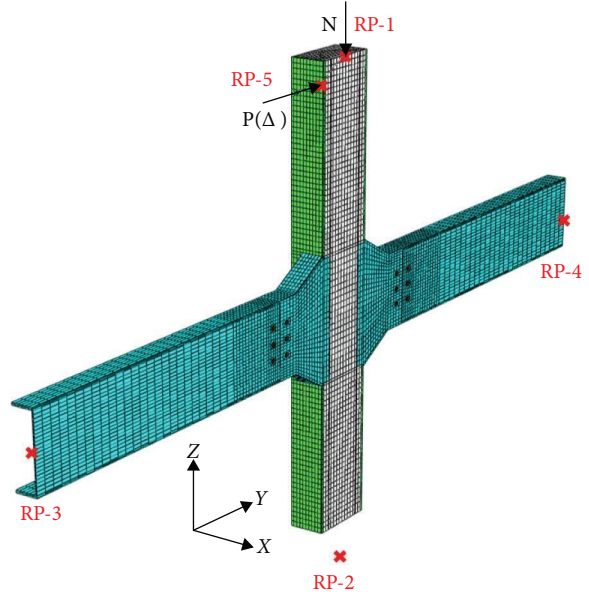

FIGURE 4: Overview of the half-model.

$$\eta = \begin{cases} 2 & \text{(concrete filled with circular steel tubes)} \\ 1.6 + \dfrac{1.5}{x} & \text{(concrete filled with square steel tubes)} \end{cases}, \tag{14}$$

3.3. Element Type and Meshes.
C3D8R was assigned to the element type of each instance in the FE model. For all instances, the structured method was chosen for the mesh generation based on detailed partition cells. The meshes in the beam-to-column conjunction area were finer than other areas because it can prevent erroneous element behavior, particularly in the key area with large deformations.

3.4. Boundary Conditions and Interaction Properties.
"Tie" constraint was used to model welding between the steel components. The surface-to-surface contact considering finite sliding was employed to model the interaction between steel and concrete. In the interaction property, "penalty" was selected as the friction formulation. The isotropic friction coefficient was 0.6 based on the FE modeling presented by

Han et al. [34], and "hard contact" was employed as the criterion of pressure–overclosure in the normal behavior. The welded vertical webs were embedded in concrete because there was no sliding and rotations between interfaces. A batch of half-models was established because boundary conditions in the test were symmetric, as shown in Figure 4.

As shown in Figure 4, coupling point RP-1 was established at the center of the column top to apply displacement constraints in the X direction and rotation constraints around the Y- and Z-axes; coupling points RP-3 and RP-4 were established at the center of the connection between the vertical hinge support and the steel beam to apply displacement constraints in the X and Z directions and rotation constraints around the Y- and Z-axes; coupling point RP-2

was established at the center of the hinge support rotation to impose displacement constraints in the X, Y, and Z directions and rotation constraints in the Y- and Z-axes.

In accordance with the test loading mode, coupling point RP-5 was established at the connection between the reciprocating actuator and the column top to apply horizontal reciprocating loads; three steps were made to apply the bolt load, axial compressive force, and cyclic lateral load in succession.

4. Analyses of Seismic Behaviors

4.1. Failure Modes.
The stress distribution and failure process of the three joint specimens were similar. The test phenomena and stress nephograms from FE analyses are shown in Figure 5. When the lateral force reached the corresponding yield load, the measured strains were almost less than 1,200 $\mu\varepsilon$, showing that steel components did not yield yet according to the material properties in the test. In the process of displacement loading, when the lateral displacements in the test reached 15–20 mm, strains of outer tubes close to the lower haunches were 1,500 $\mu\varepsilon$, which approximated the yield strain of the steel tube. Figure 5(a) shows that stresses at this corresponding position exceed yield strength at this moment. When the lateral displacements in the test increased to 24–28 mm, peeling of the steel beam surface was captured, as shown in Figure 5(b), since a layer of oxide on the steel surface cracked and fell off with the increase of steel deformation, and the drop of steel chips on the flange surface became more obvious. Then, the beam flange strain was measured to reach the yield value. Likewise, the stress nephogram displays stresses at the corresponding position larger than that in the vicinity. The loading force continued to increase, and it reached the ultimate bearing capacity at the lateral displacements of 37–41 mm. Afterward, the beam flange slowly bulged, and the test photo together with the FE stress nephogram is shown in Figure 5(c) at the lateral displacements of 42–54 mm. At the end of the loading, the butt weld cracked in the test and the stress of this part of steel obtained by FE analysis is over ultimate stress, as shown in Figure 5(d). The cracking of the butt weld does not affect the failure mode of the joint because the steel beam bents first to form the plastic hinge, as shown in Figure 5(c), and the fracture of the brittle butt weld is caused by the larger plastic deformation of the steel. The final failure mode of the joint in both the test and FE analysis, as shown in Figure 6, was plastic hinges at steel beam ends, and the failure occurred primarily in the beam. It attributes that the haunched joint with ribbed anchor webs builds a strong connection with the CFDST column. In the test, the strain gauge readings of beam-to-column rotation and panel zone's shear deformation were very small. In the FE simulations, shear stress distribution in the panel zone was almost in an elastic state, and Mises stress exceeded the ultimate strength only at the zone where the beam flange was away from the haunch. Therefore, the configurations of the haunched joint with ribbed anchor web form a triangular strengthened joint core to guarantee the rigid beam-to-column connection.

4.2. Strain and Stress Responses.
There was no significant difference in strains of outer steel tubes of the three specimens, but it was different for strains of inner steel tubes of specimens SPJ2 and SPJ3 in the case of the same steel beams. The general relation between the lateral force (P) and strain (ε), including vertical strains and circumferential strains from the upper measuring point on the inner tube, can be reflected by skeleton curves, as shown in Figure 7. In addition to identical ribbed anchor webs, additional stiffening diaphragms were installed in specimen SPJ3 (see Figures 1(b) and 1(c)). Compared to SPJ2, the strains in the inner steel tube of SPJ3 were much higher and exceeded the yield strain. It was attributed that the stiffening diaphragms were conducive to shifting internal force from beam ends to inner steel tubes, and the connected inner tube in SPJ3 worked sufficiently, so that the internal force could be effectively distributed in a larger area of the inner tube rather than limited to the joint core area. Figure 8 shows stress nephograms of the two FE models at the peak state, and it also proves that the stress distribution in SPJ3 is more uniform than that in SPJ2 due to the configuration of stiffening diaphragms, and stresses in ribbed anchor webs of SPJ2 are much larger than that of SPJ3. In brief, cross-sectional characteristics of the CFDST column were exerted effectively to redistribute the internal force in the panel zone for the haunched joint with ribbed anchor webs, especially for that with stiffening diaphragms.

4.3. Hysteretic Curves.
The force (P)–displacement (Δ) hysteretic curves obtained from tests and FE analyses are shown in Figure 9, and the latter is basically consistent with the former. In the elastic stage, there is little change in the initial stiffness of each joint specimen, and the displacement linearly increases with the force. In the deformation development stage, hysteretic curves gradually change to be full and are hardly pinched, showing that the joint possesses sufficient energy dissipation performance. As the applied displacement increases, stiffness degenerates steadily due to increased curvature of bending beam flanges near haunches. Strain gauge readings showed that except the stress concentration on the outer tube near the haunch, deformation development mainly focused on the beam flange, so the lateral displacement at the peak point of the three specimens is relatively small (about 40 mm). It shows that the haunched joint with ribbed anchor webs has large stiffness to restrict the ultimate deformation of the connection. As for the failure stage, the measured force drops sharply as the lateral displacement increases owing to the fracture of butt welds in beam flanges, so the stiffness and strength degradation observed after the peak force in the test are not realistic enough because the joint has high requirements for weld quality, which were not met under our test conditions. The last stage of hysteretic curves obtained from FE analyses decreases slowly. Although there are a few differences in later load–deformation development between tests and FE analyses, both are mutually validated with respect to the failure process, initial stiffness, ultimate resistance capacity, and hysteretic curve shape. It was considered that the numerical
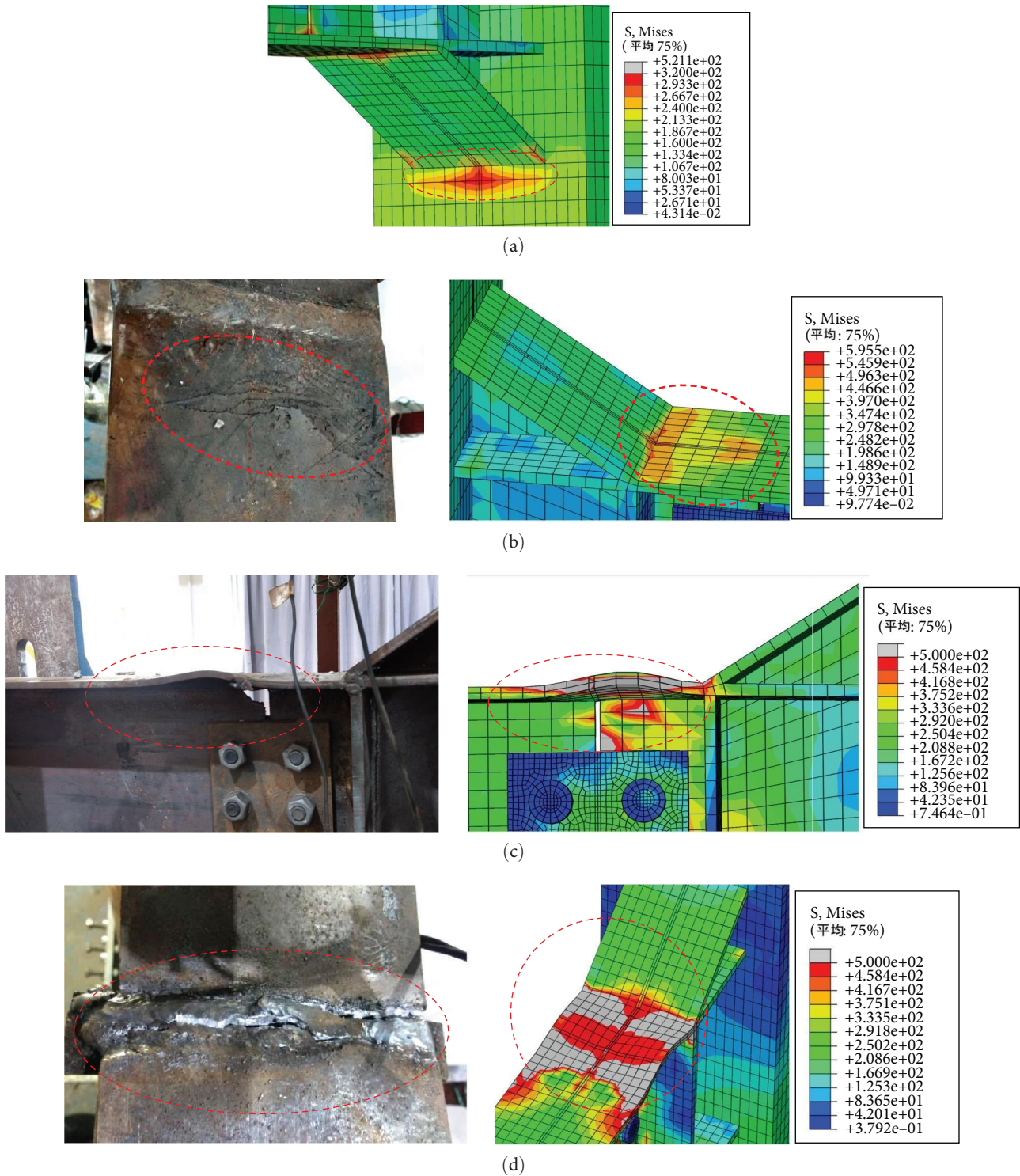
(a)

(b)

(c)

(d)

FIGURE 5: Test phenomena and corresponding stress nephograms. (a) Yielding at the junction between the lower haunch and the column. (b) Peeling phenomenon and the corresponding stress nephogram. (c) Bulging beam flange and the captured phenomenon. (d) Welding cracks and the corresponding stress nephogram.

model is adequate for the aftermentioned parametric analysis.

4.4. Skeleton Curves. The skeleton curves obtained from tests and FE analyses are shown in Figure 10, and it can be seen that the curves obtained from FE analyses are symmetric based on the origin. The initial stiffness and ultimate bearing capacity obtained from tests or FE analyses are very close. The mean error of the ultimate bearing capacity between FE analyses and tests is 2.09%; the maximum error is 2.77%. Synthesizing the positive direction and the negative direction of skeleton curves from the test, the force and displacement
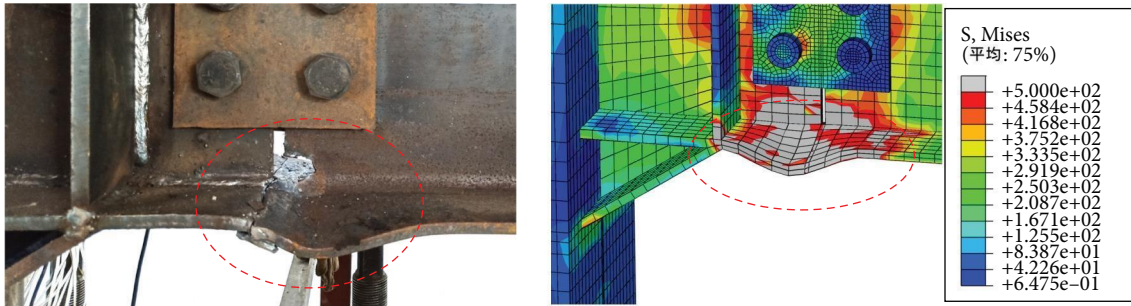
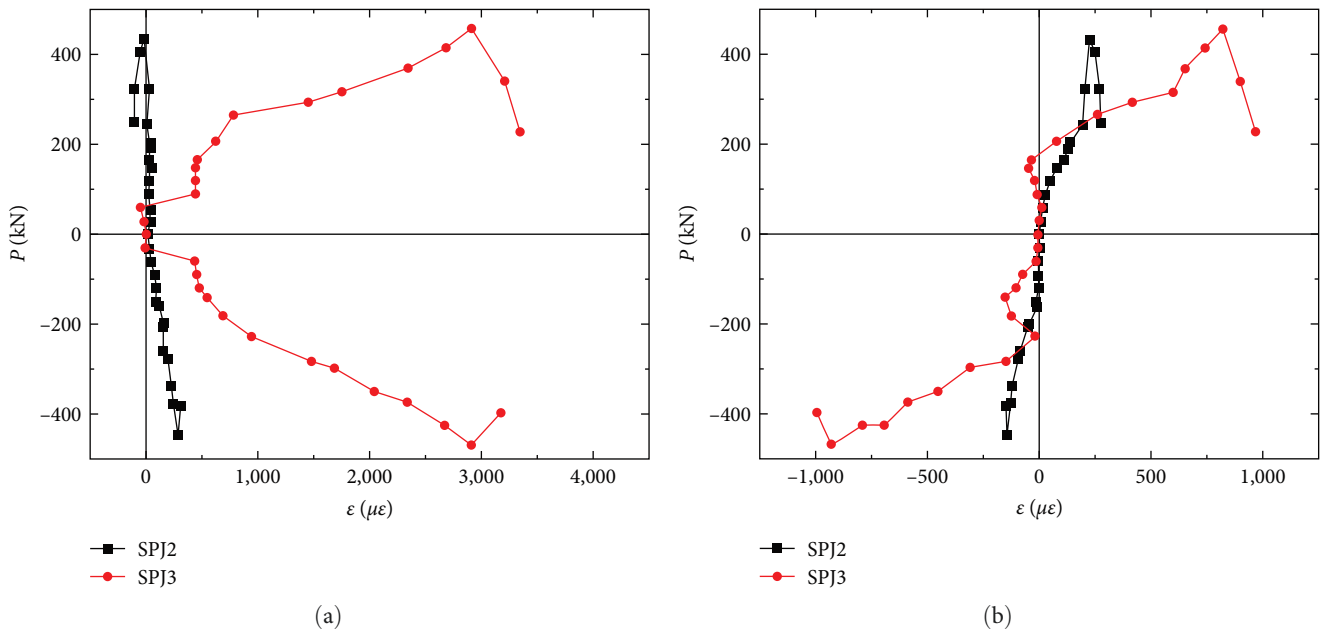FIGURE 6: Final failure mode in the test and the FE analysis.

(a)

(b)

FIGURE 7: P–ε skeleton curves. (a) Vertical strains of inner steel tubes. (b) Circumferential strains of inner steel tubes.

corresponding to each characteristic point, and ductility factors are shown in Table 3. The ductility factor (u) for evaluating the ductility of the structure is a ratio of the failure displacement (Δ_d) divided by the nominal yield displacement (Δ_y), i.e., $u = \Delta_d/\Delta_y$. A typical P–Δ skeleton curve and relevant characteristic points are shown in Figure 11. P_y, P_{max}, and P_d, respectively, denote the nominal yield force, the peak force, and the failure force. The average ductility factor derived from tests is 2.21, and it is smaller than what was derived from FE analyses because the weld defects and the residual stress in weld seams made specimens easy to fail in tests. The test data show that the ultimate bearing capacity of specimen SPJ2 is 16.38% higher than that of specimen SPJ1 because the cross-sectional dimensions of the steel beams in SPJ2 are larger. The ultimate resistance capacity of SPJ3 with stiffening diaphragms is enhanced by 5.58% than that of specimen SPJ2, so though stiffening diaphragms with a small cross-sectional area were installed only between double tubes, it still improved the ultimate strength of the joint.

4.5. Energy Dissipation Performance. The equivalent viscous damping coefficient h_e is utilized to assess the energy dissipation performance. For each specimen, changes of h_e at each cycle number are shown in Figure 12, where i represents the number of half hysteresis loops. At the failure point, h_e is 0.273, 0.280, and 0.295 for SPJ1, SPJ2, and SPJ3, respectively. The energy dissipation of specimens rose with the increase of the loading loop, proving that plastic hinges at beam ends absorbed a lot of energy. The curves show that the energy dissipation capacity of SPJ2 is basically equal to that of SPJ1, but the energy dissipation capacity of SPJ3 is much greater than that of SPJ2. Therefore, an increase in cross-sectional dimensions of the steel beam only had a slight improvement in the energy dissipation capacity owing to the same connection construction, while installing the anchor component such as stiffening diaphragms contributed to the improvement of energy dissipation capacity. Therefore, although the stiffening diaphragm between the double tube has a small cross-section, it can make good use of the special sectional
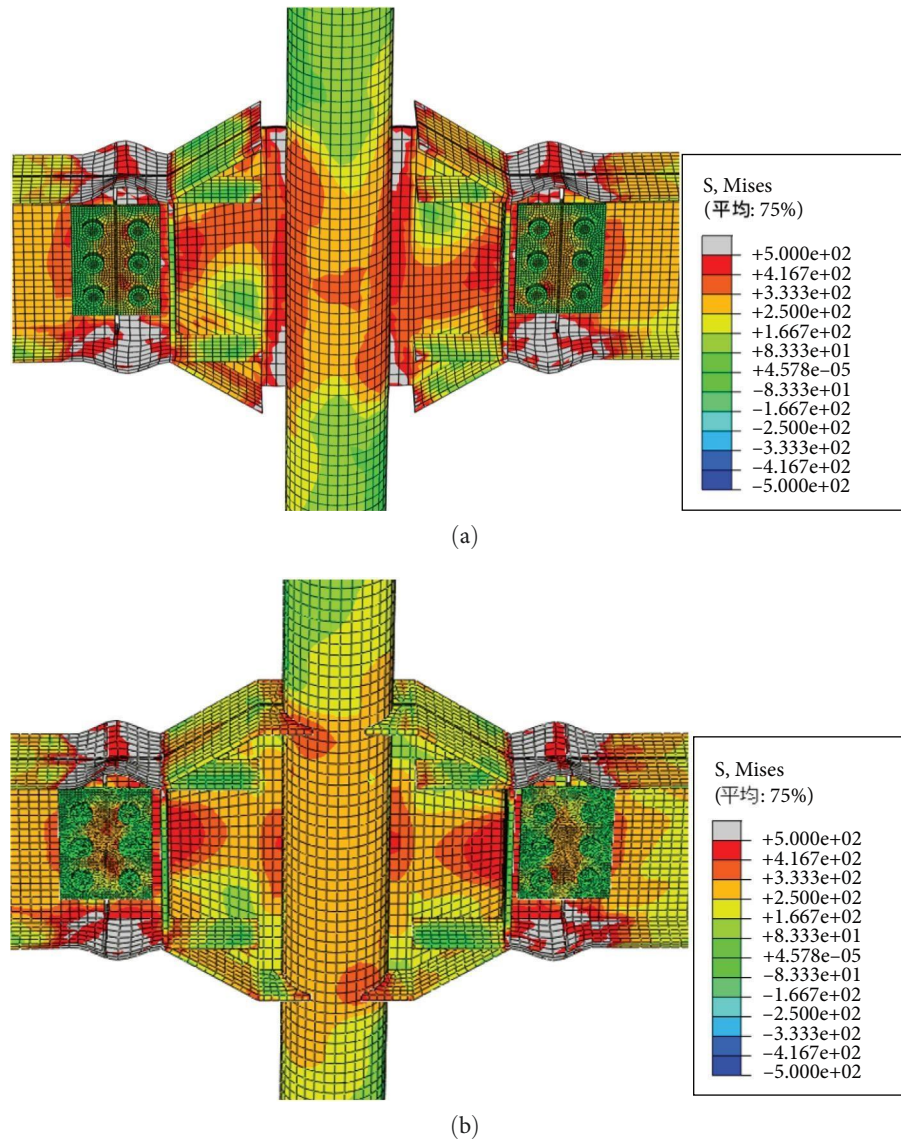
(a)

(b)

FIGURE 8: Stress nephograms of the joint core area. (a) SPJ2 (without stiffening diaphragms). (b) SPJ3 (with stiffening diaphragms).

characteristic of CFDST column to aim at the improvement of energy dissipation for this type of joint.

5. Parametric Analyses

A series of FE models was established to further analyze how different parameters affect seismic behaviors of the proposed joint type. The selected parameters include configurations, geometric dimensions, material strength of steel and concrete, and axial compression ratios (n), as shown in Table 4. In every group, the superscript "∗" represents the parameter derived from the test specimen SPJ2, and other corresponding parameters were changed based on specimen SPJ2. The first quadrant of P–Δ skeleton curves obtained by FE analyses was used for parametric analyses due to the symmetry.

5.1. Influences of Constructional Details. For model SPJ2-H, haunches were removed, and vertically ribbed webs were direct force-transferring elements, while there were no ribs

and haunches for model SPJ2-HS. Figure 13 shows different failure modes of these three models. The bulging column and the plastic hinges close to the CFDST column were captured on model SPJ-HS. For model SPJ-H, bulges of the column were effectively alleviated, and the plastic hinges were shifted outside. Besides, the ribs had small bulges along the hypotenuse, which absorbed a part of energy during the cyclic loading process. For model SPJ2, an ideal failure mode of plastic hinges formed at beam ends was captured as expected. Meanwhile, the stress concentration at the core area significantly decreased and there were no bulges on the outer steel tube. P–Δ hysteretic curves, as shown in Figure 14, present different degrees of full loops, and h_e is 0.139, 0.438, and 0.161, respectively, for models SPJ2-HS, SPJ2-H, and SPJ2 at the peak load point. Although the vertically ribbed web joint has a higher energy dissipation capacity, the column and panel zone made contributions to the energy dissipation due to large deformations, which can't meet the
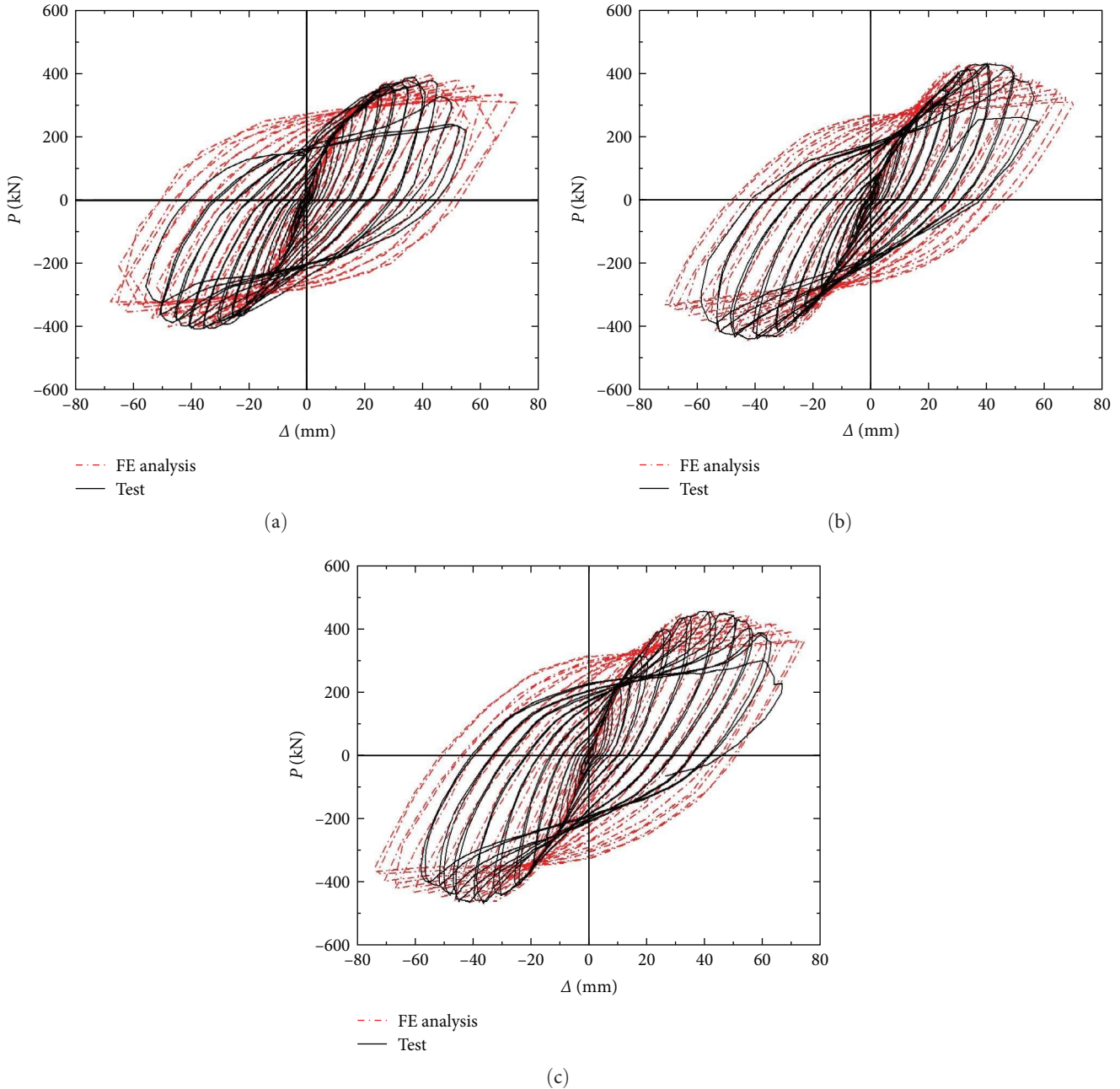
(a)

(b)

(c)

FIGURE 9: Comparisons of P–Δ hysteretic curves between tests and FE analyses. (a) Specimen SPJ1. (b) Specimen SPJ2. (c) Specimen SPJ3.

engineering requirements of strong joints. The skeleton curves, as shown in Figure 15, show that initial stiffness of model SPJ2 was improved by 15.91% more than that of model SPJ2-H and was improved by 52.96% more than that of model SPJ2-HS. The ultimate bearing capacity was increased by 31.42% and 69.60% correspondingly. The contrastive analysis demonstrates that haunches and ribs have constructive effects on seismic behaviors of the haunched joint under cyclic loading.

5.2. Influences of Beam-to-Column Bending Stiffness Ratios Per Unit Length (k). The beam-to-column bending stiffness ratios per unit length (k) for parametric analyses were 0.3,

0.41, 0.5, and 0.6. Herein, k was designed by changing the length of the steel beam, and the beam length was 5,057, 3,700, 3,034, and 2,528 mm, respectively. The cross-sectional dimension of the beam was H $350 \times 175 \times 7 \times 11$. The failure mode of all FE models was ideal, as plastic hinges captured at beam ends. Figure 16 shows corresponding P–Δ skeleton curves obtained from FE analyses. It indicates that the ultimate bearing capacity and initial stiffness improve with the increase of k because the rotation stiffness of the beam would be strengthened when k is large. When $k = 0.41$, 0.5, and 0.6, the ultimate resistance capacity was improved by 9.88%, 15.55%, and 16.77%, respectively, in comparison with the model of $k = 0.3$, and initial stiffness was improved by
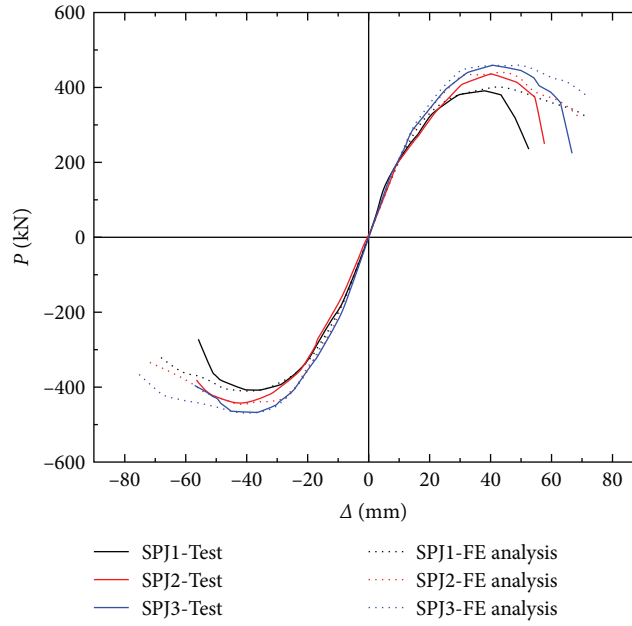
FIGURE 10: P–Δ skeleton curves.

TABLE 3: Bearing capacity and ductility factors of each specimen.

| Specimen			Yield point		Peak point		Failure point		u
			P_y (kN)	Δ_y (mm)	P_{max} (kN)	Δ_m (mm)	P_d (kN)	Δ_d (mm)	
SPJ1	FE analysis		349.8	24.2	400.6	43.6	320.4	70.4	2.91
	Test	Push	343.4	22.7	390.0	38.4	276.4	45.3	2.00
		Pull	369.8	25.1	407.6	35.7	326.1	52.8	2.10
SPJ2	FE analysis		408.7	25.5	440.1	44.0	352.1	64.7	2.54
	Test	Push	370.9	26.3	436.1	40.2	348.9	55.2	2.10
		Pull	393.0	27.6	440.5	39.5	352.4	57.7	2.09
SPJ3	FE analysis		417.4	26.5	459.5	50.2	367.6	72.8	2.75
	Test	Push	395.3	26.1	457.1	40.6	366.1	62.4	2.39
		Pull	418.9	25.9	468.4	36.7	374.7	58.1	2.24
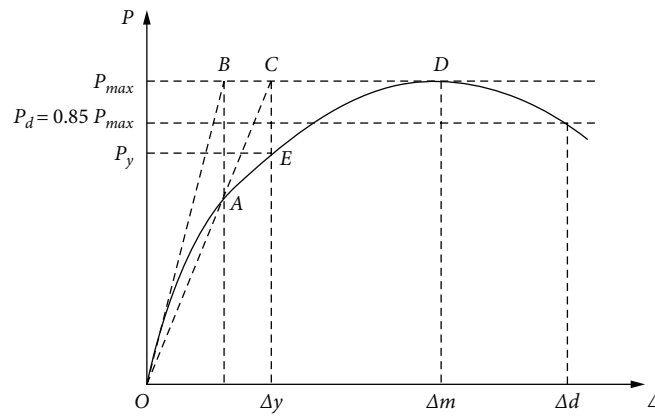
FIGURE 11: Characteristic points in the typical P–Δ skeleton curve.
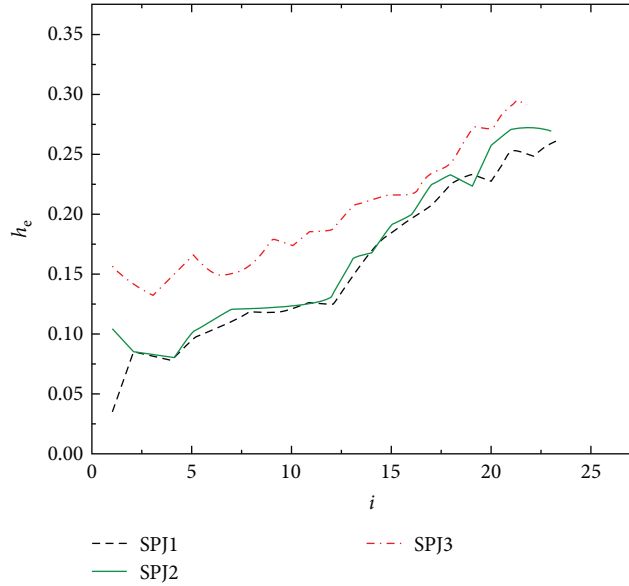
FIGURE 12: Changes of equivalent viscous damping coefficients (h_e) at each half-cycle number (i).

TABLE 4: Parameter settings.

Types	Parameters	Contents
	Both ribs and haunches	SPJ2*
Configurations	Only ribs	SPJ2-H
	No ribs and no haunches	SPJ2-HS
Geometric dimensions	Beam-to-column bending stiffness ratios per unit length (k)	0.3, 0.41*, 0.5, 0.6
	Steel beam strength	Q235*, Q345, Q420, Q550
Material strength	Concrete strength	C40, C50, C60*, C80, no concrete
Compressive force on the column top	Axial compression ratios (n)	0.04, 0.275*, 0.4, 0.5, 0.6

6.03%, 32.51%, and 42.45% correspondingly. The differences in the two indexes between models of $k = 0.5$ and $k = 0.6$ were not evident, so the value of k from 0.3 to 0.5 is fit for this joint type to perform excellent seismic behaviors.

5.3. Influences of Steel Beam Strength. The steel grade of the steel beam was Q235 in the test, and Q345, Q420, and Q550 were further considered in FE analyses. Figure 17 shows P–Δ skeleton curves of corresponding joint models labeled by Q345, Q420, and Q550. The nominal yield displacements increased successively with the increasing steel beam strength, and the ultimate resistance capacity of models Q345, Q420, and Q550 was, respectively, improved by 17.32%, 27.77%, and 47.94% more than that of model Q235. However, initial stiffness was equal since cross-sectional dimensions and Young's modulus of all steel beams were unchanged, and the ductility was decreasing with larger steel beam strength. Figure 18 shows stress nephograms of Models Q420 and Q550 at the peak point, and it can be found that stresses in ribbed anchor webs, steel beams, and outer steel tubes rise significantly when steel beam strength

increased, and it caused larger deformations at beam flanges. For model Q550, the failure mode also includes local buckling of the outer tube wall. Then, according to constructional details of the specimen SPJ3, stiffening diaphragms were added on model Q550 to form the new model Q550+, and its failure mode is shown in Figure 18(c). The whole CFDST column worked as a whole through stiffening diaphragms between two tubes. Meanwhile, the stress concentration area and the bulging part of the outer tube were reduced, and the ductility was also better than that of model Q550 because the internal force from beams was more effectively transmitted to the joint core via stiffening diaphragms. The bearing capacity of model Q550+ was improved by 7.65% more than that of model Q550. Therefore, it is practicable to install stiffening diaphragms to enhance ductility and bearing capacity, especially when the steel beam strength is large.

5.4. Influences of Concrete Strength. The uniaxial compressive strength of concrete cubes was selected as 40, 50, 60, and 80 MPa to compute the constitutive relation and model the
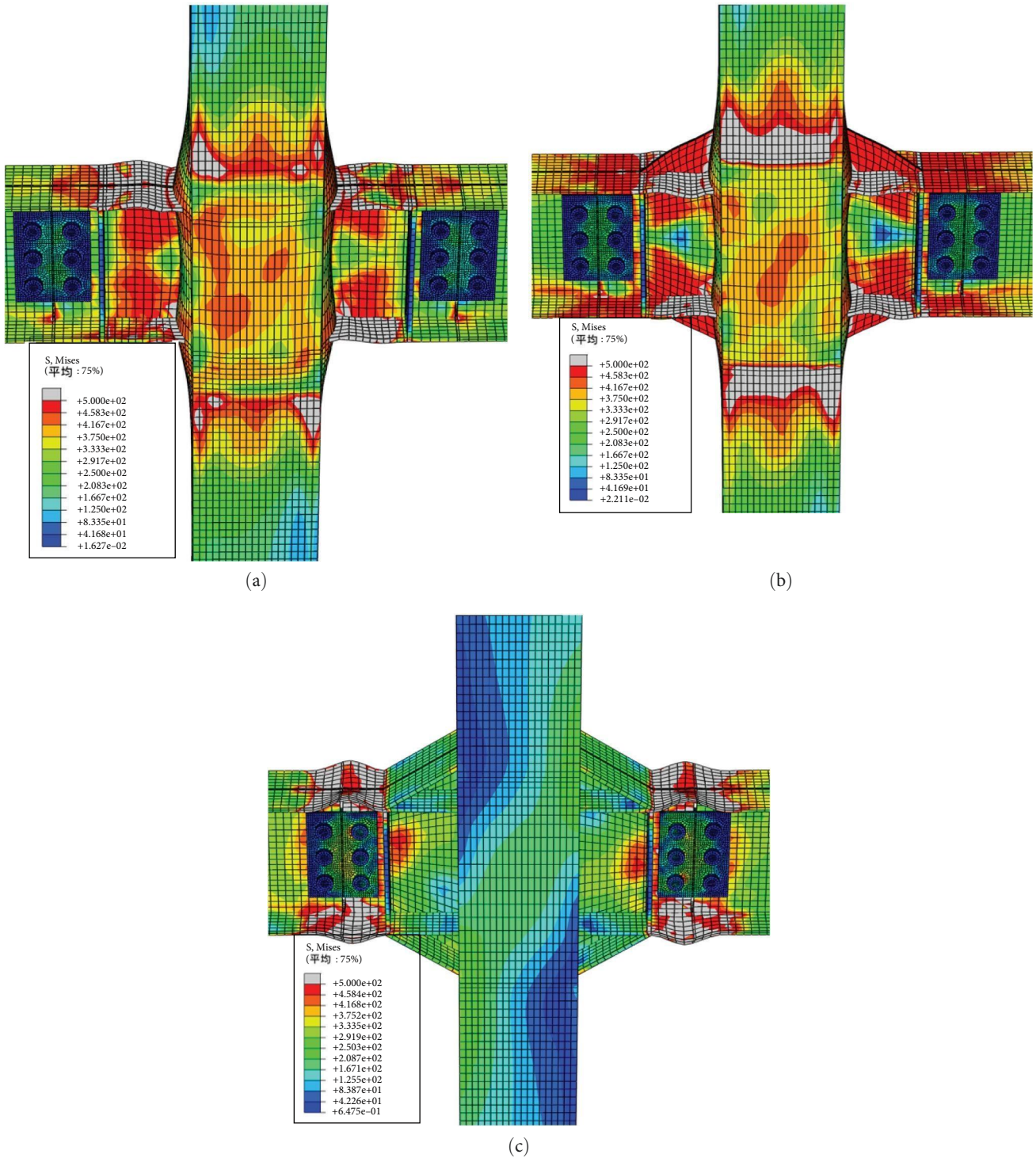
(a)

(b)

(c)

FIGURE 13: Stress nephograms of joint models with different constructional details. (a) Model SPJ2-HS. (b) Model SPJ2-H. (c) Model SPJ2.

different joints, and a model without concrete was adopted for comparison. All the models were labeled by the different concrete C40–C80 and no concrete. Figure 19 shows the P–Δ skeleton curve of each joint model. There was a sharp degeneration in initial stiffness and ultimate resistance capacity for model no concrete because concrete can improve the rigidity of the column and the globality of the joint. The initial

stiffness and the ultimate resistance capacity of model C40 were 102.87% and 112.46%, respectively, higher than those of model no concrete. However, there was a slight improvement in initial stiffness and ultimate bearing capacity when concrete strength increased. The stress nephograms and failure modes of models C40, C50, C60, and C80 were extremely similar, so stress nephograms of model C40 and model no
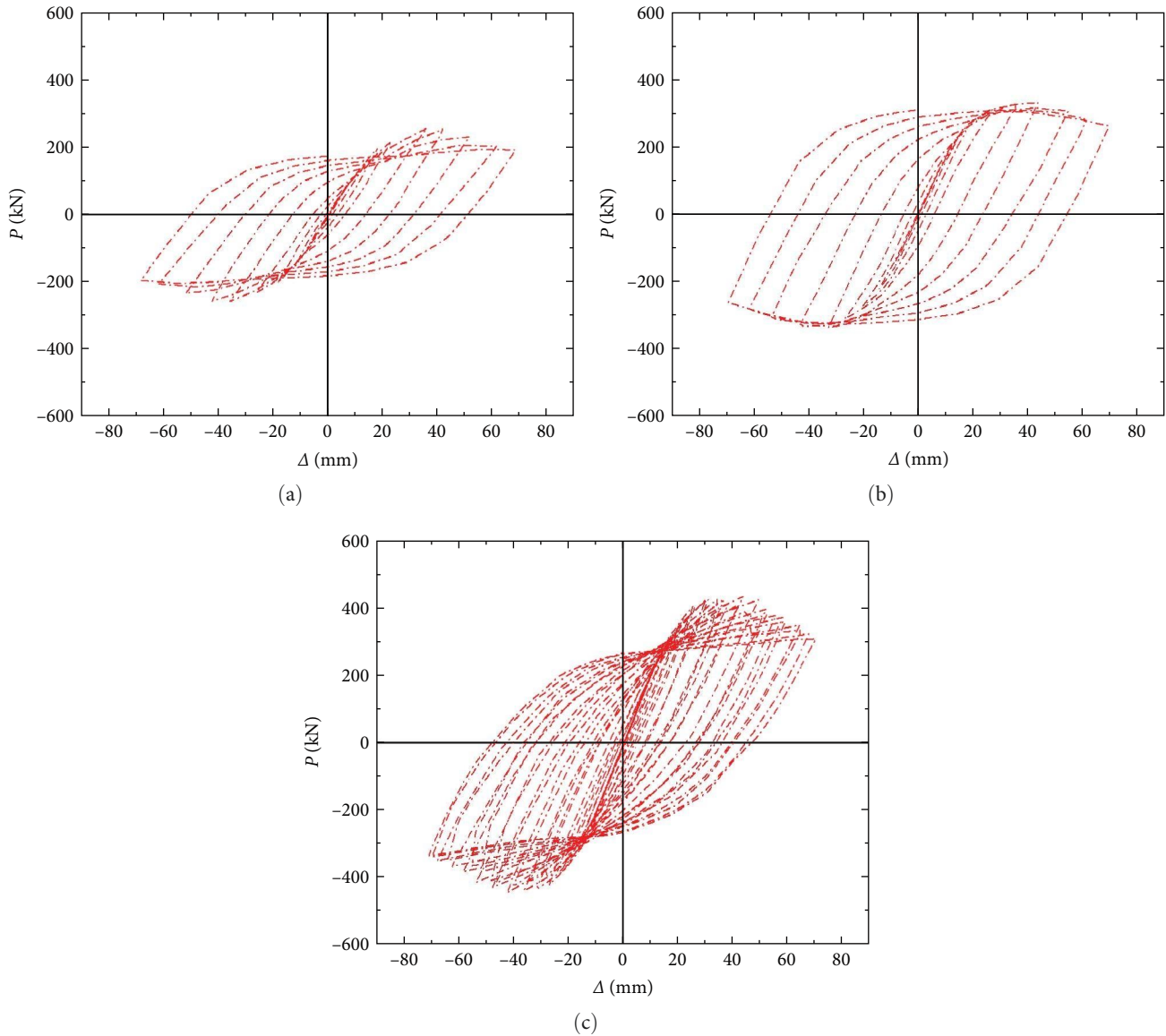
(a)

(b)

(c)

FIGURE 14: P–Δ hysteretic curves of joint models with different constructional details. (a) Model SPJ2-HS. (b) Model SPJ2-H. (c) Model SPJ2.

concrete are shown in Figure 20. The column of model no concrete bulges, and the bulging position is near the haunch since the hollow thin-walled column under compression is prone to instability and buckling, especially for the area of sudden changes in bending stiffness. In the final failure stage, the steel beam was still in a good state without stress concentration and large deformation when the column failed (Figure 21(b)). It is concluded from this contrastive analysis that the haunched joint with ribbed anchor webs for the CFDST structure is applicable and using low-strength concrete to reduce the construction budget based on engineering requirements is practicable.

5.5. Influences of Axial Compression Ratios (n). The axial compressive force on the CFDST column is an important factor affecting joints' seismic performance. The values of n were considered as 0.04, 0.275, 0.4, 0.5, and 0.6 in FE analyses.

Figure 21 shows corresponding P–Δ skeleton curves. The results illustrated that n influenced joint initial stiffness, ultimate resistance capacity, ductility, and deformation resistance. When $n = 0.275$, 0.4, 0.5, and 0.6, initial stiffness was enhanced by 25.08%, 59.82%, 87.49%, and 162.70%, respectively, in comparison with that of model of $n = 0.04$. As for the ultimate resistance capacity, it enhanced 6.21%, 7.71%, 15.64%, and 21.60%, respectively. It was attributed that the confinement effect to concrete from double steel tubes was enhanced with the increase of axial compressive force. Accordingly, there was a sharper fall in the P–Δ skeleton curve after each peak point with the increase of the axial compressive force, showing a decrease indeformation resistance and ductility. When $n = 0.04$, 0.275, and 0.4, failure modes of the joint models were that plastic hinges generated at beam end, while failure modes of the joint models were the buckling failure of the CFDST column and
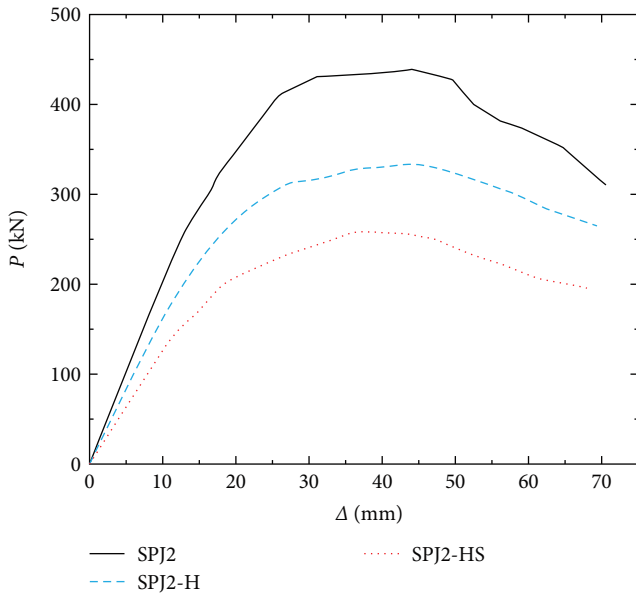
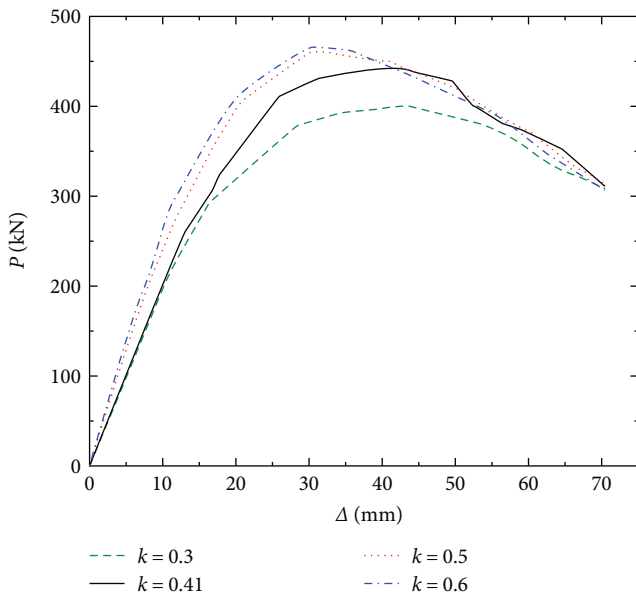FIGURE 15: P–Δ skeleton curves of joint models with different constructional details.

FIGURE 16: P–Δ skeleton curves of joint models with different beam-to-column bending stiffness ratios per unit length (k).

FIGURE 17: P–Δ skeleton curves of joint models with different steel beam strength.

bulge phenomena on the outer tube wall when $n = 0.5$ and 0.6. These differences are shown in Figure 22. Therefore, the axial compression ratio under 0.5 is better to prevent the buckling failure and bulges of the CFDST column, so as to guarantee sufficient ductility in seismic designs for the haunched joint with ribbed anchor webs.

6. Conclusions

Three haunched joints with ribbed anchor webs were tested under lateral cyclic loads, and failure modes, strain and stress responses, hysteretic 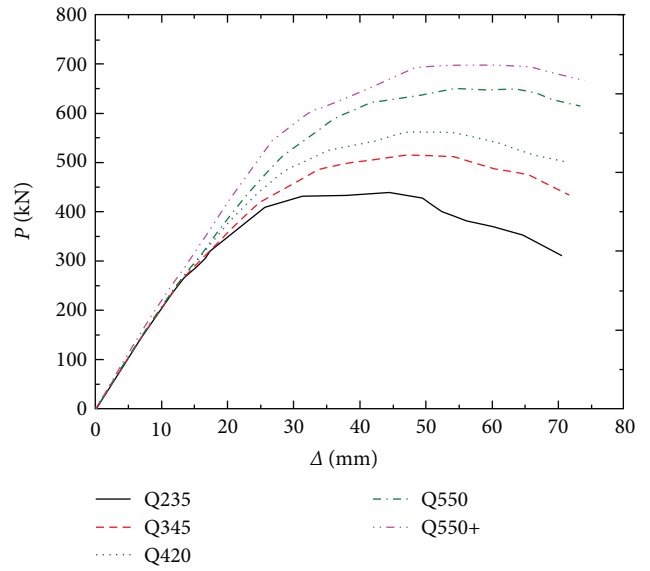curves, and energy dissipation performance were analyzed. The effective constitutive relations of materials, the reasonable element type and meshes, the identical boundary conditions, and appropriate interactions were selected to conduct FE analyses by ABAQUS program. FE analyses were validated by test results, and then a series of parametric analyses was carried out. The main conclusions are as follows:

(1) Failure mode of the haunched joint with ribbed anchor webs was plastic hinges at steel beam ends. The position was far from the joint core area owing to the installation of haunches. The deformation in joint specimens concentrated at steel beams and there was a little damage to columns, which indicated that this connection type for the CFDST column met the criterion of "strong column and weak beam." The hysteretic curves were full and there was almost no pinch phenomenon, which manifested that the tested joints had excellent energy dissipation capacity. The ultimate bearing capacity was increased with the improvement of cross-sectional dimensions of the steel beam; stiffening diaphragms with a small cross-sectional area can improve the ultimate strength of the joint and especially improve ductility and energy dissipation capacity particularly.

(2) FE analysis results coincided with test results with respect to the failure process, hysteretic curves, and skeleton curves. Parametric analyses showed that besides ribs and haunches, stiffening diaphragms are practicable to connect the double tubes, especially for the high-strength steel beam; beam-to-column bending stiffness ratio per unit length is appropriate to be 0.3–0.5 to exert good mechanical performances; choosing low-strength grade of concrete is allowed to satisfy engineering requirements; the axial compression ratio should be limited within 0.5. The synthetic analyses further confirmed that the proposed joint type behaved as a rigid connection with good seismic behaviors.
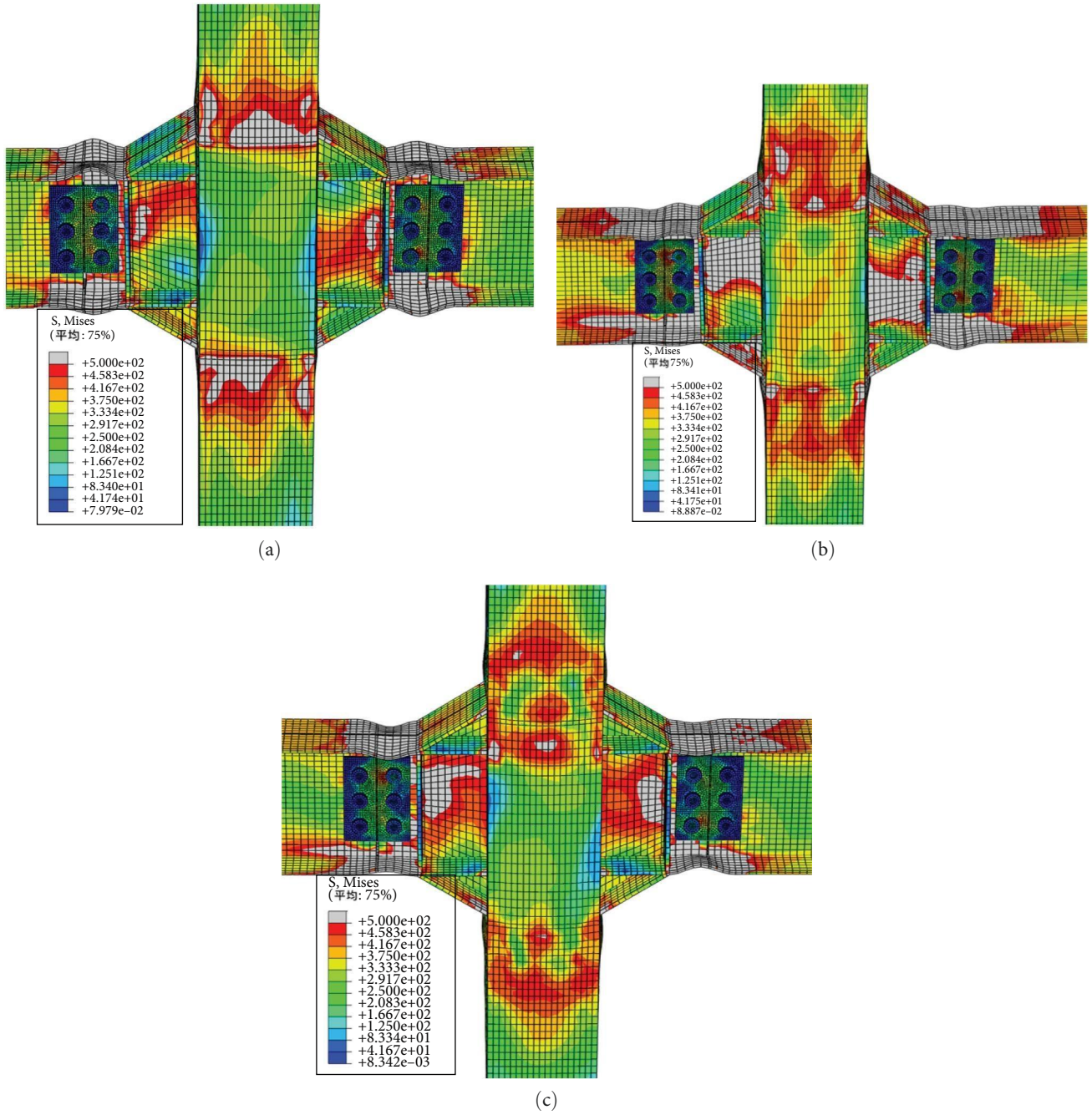
(a)

(b)

(c)

FIGURE 18: Stress nephograms of joint models with different steel beam strength. (a) Model Q420. (b) Model Q550. (c) Model Q550+.
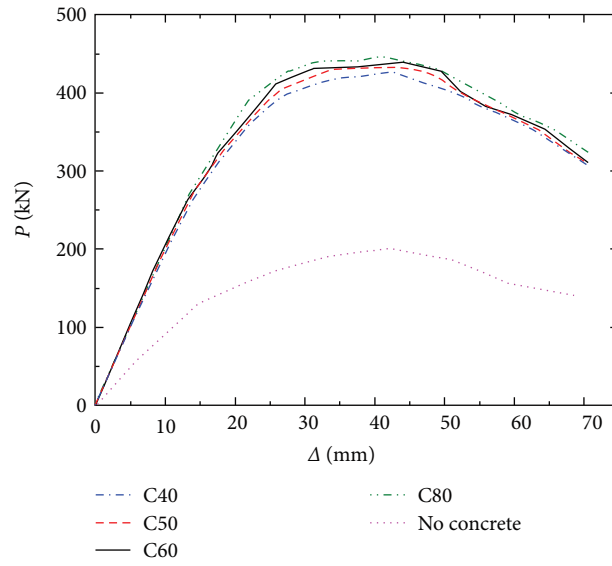
FIGURE 19: *P*–*Δ* skeleton curves of joint models with different concrete strength.
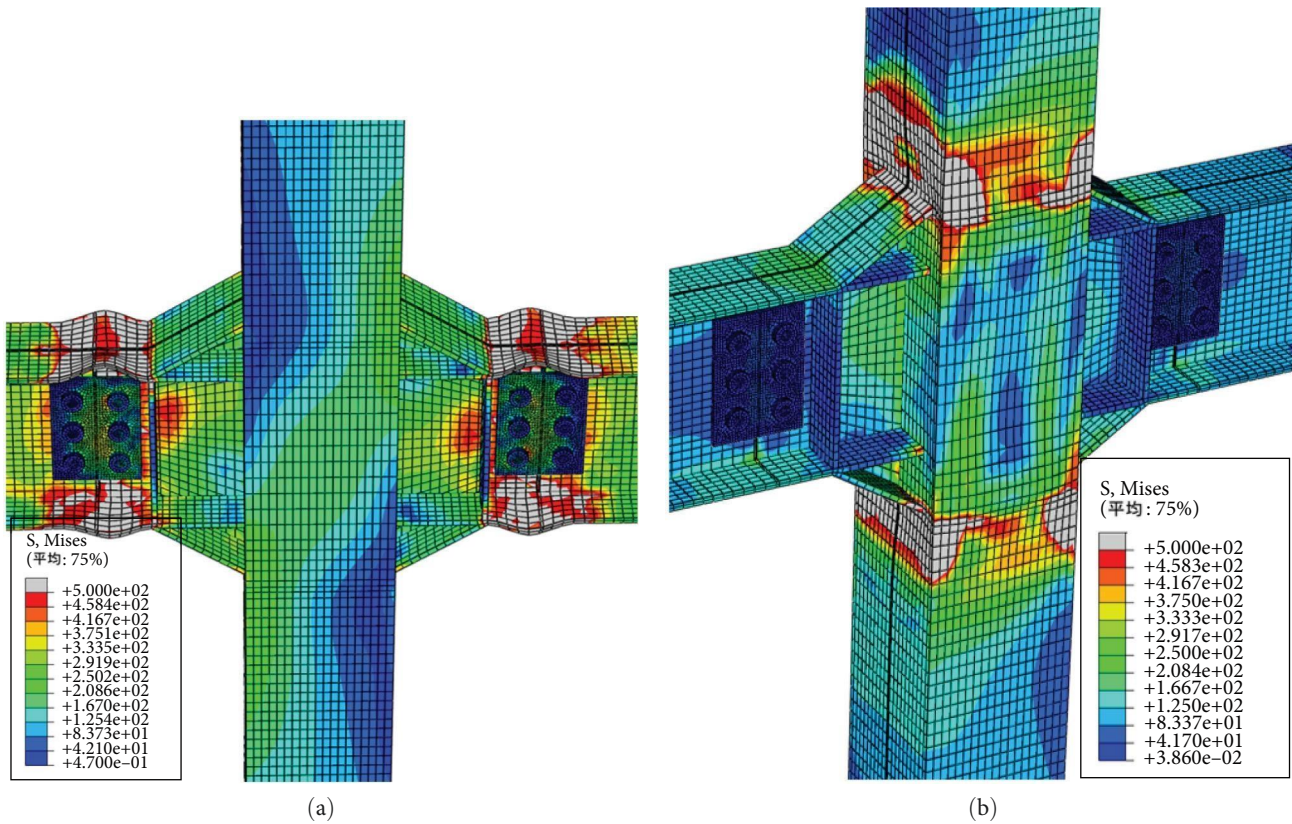

FIGURE 20: Stress nephograms of joint models with different concrete strength. (a) Model C40. (b) Model no concrete.
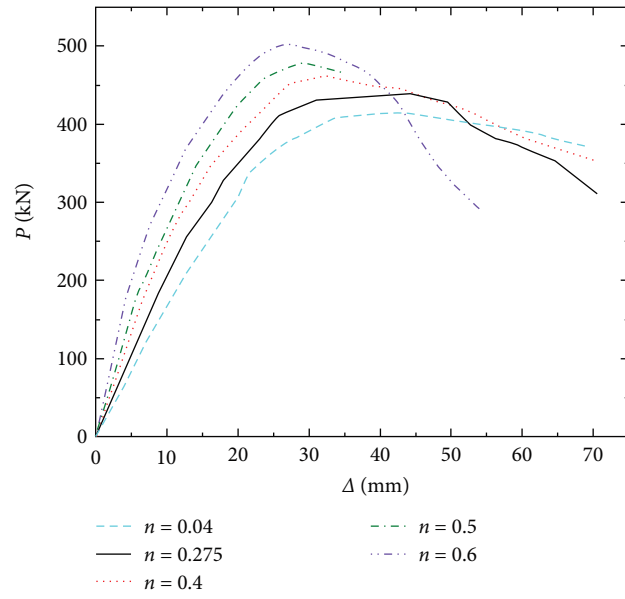
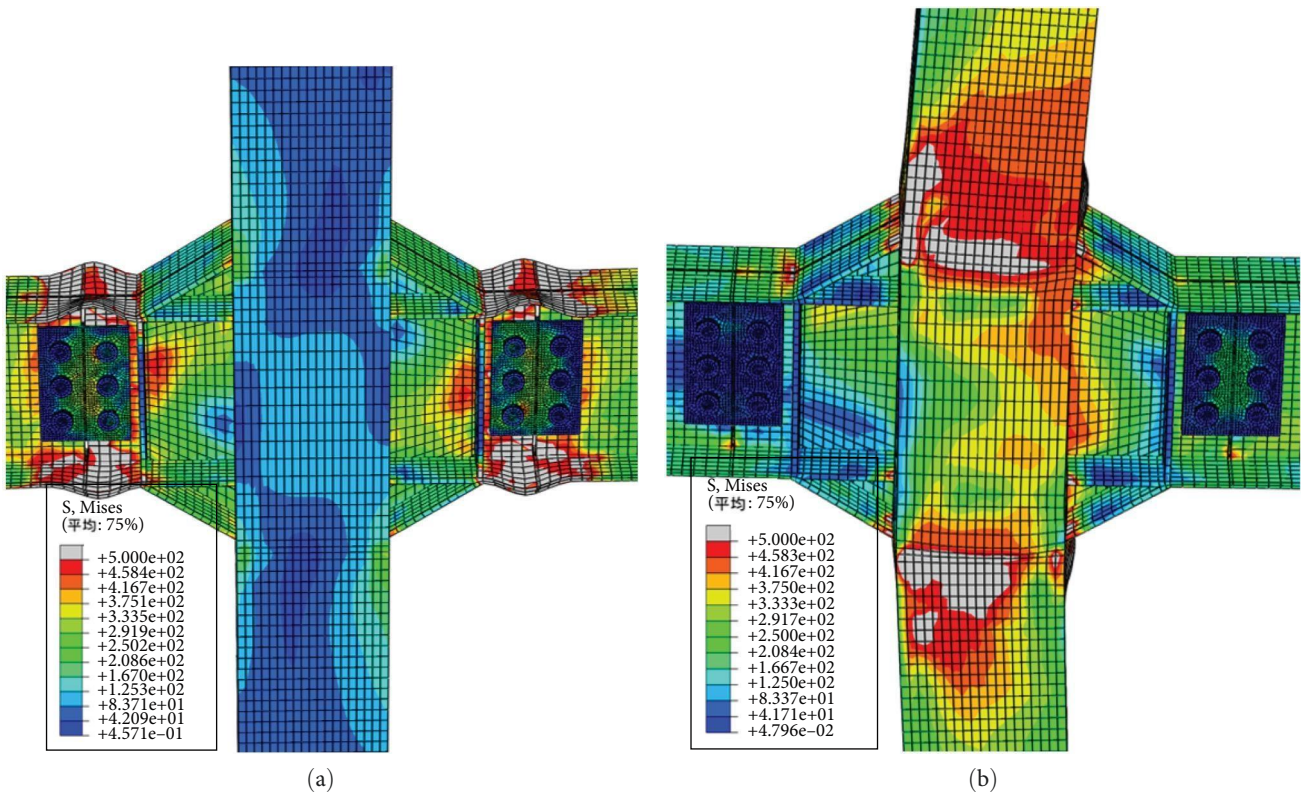FIGURE 21: P–Δ skeleton curves of joint models with different axial compression ratios (n).

FIGURE 22: Two typical failure modes of joint models with different axial compression ratios (n). (a) $n = 0.04$. (b) $n = 0.6$.

Data Availability

The data used to support the findings of this study are available from the corresponding author upon request.

Disclosure

A preprint has previously been published in Research Square [35], and this is an updated version of the manuscript.

Conflicts of Interest

The authors declare that they have no conflicts of interest.

Authors' Contributions

Conceptualization, Yufen Zhang and Shengxi Cao; writing—review and editing, Xiaokun Qu; project administration, Ling Wang; writing—original draft preparation, Hongfan Bu; resources, Shengxi Cao; funding acquisition, Yufen Zhang. All authors have read and agreed to the published version of the manuscript.

Acknowledgments

References

[1] J. C. Ci, A. Mizan, D. X. Zhou, L. Q. Hou, and S. C. Chen, "Flexural performance of circular concrete-filled double steel tubular members: testing, modeling, and strength predictions," *Structural Concrete*, vol. 24, no. 1, pp. 818–839, 2022.

[2] H. Huang, L.-H. Han, and X.-L. Zhao, "Investigation on concrete filled double skin steel tubes (CFDSTs) under pure torsion," *Journal of Constructional Steel Research*, vol. 90, pp. 221–234, 2013.

[3] M. Li, Z. Zong, H. Hao, X. Zhang, J. Lin, and G. Xie, "Experimental and numerical study on the behaviour of CFDST columns subjected to close-in blast loading," *Engineering Structures*, vol. 185, pp. 203–220, 2019.

[4] J. Wang, X. Cheng, C. Wu, and C.-C. Hou, "Analytical behavior of dodecagonal concrete-filled double skin tubular (CFDST) columns under axial compression," *Journal of Constructional Steel Research*, vol. 162, no. 8, pp. 584–597, Article ID 105743, 2019.

[5] M. Ehsan, M. Maeve, and J.-W. Hu, "Environmentally friendly concrete compressive strength prediction using hybrid machine learning," *Sustainability*, vol. 14, no. 20, Article ID 12990, 2022.

[6] L.-H. Han, *Concrete Filled Steel Tubular Structures—Theory and Practice*, Science Publishing & Media Ltd., Beijing, China, 3rd edition, 2016.

[7] Y. Hu, J. Zhao, D. Zhang, and C. Chen, "Experimental seismic performance of CFDST-steel beam frames with different construction details," *Journal of Constructional Steel Research*, vol. 162, pp. 613–627, Article ID 105736, 2019.

[8] Q. Yan, J. Zhang, F. Liu et al., "Experimental and numerical study on the dynamic behavior of concrete-filled double steel tubular T-joint under impact loading," *Ocean Engineering*, vol. 269, Article ID 113509, 2023.

[9] Y. Zhang, D. Zhang, and K. Demoha, "Internal force transfer mechanism and bearing capacity of vertical stiffener joints in CFDST structures," *Advances in Materials Science and Engineering*, vol. 2019, Article ID 2105365, 12 pages, 2019.

[10] Y. Zhang, H. Jia, Y. Li, and K. Demoha, "Experiments on cyclic performance of external diaphragm joints between CFDST columns and steel beams," *Bulletin of Earthquake Engineering*, vol. 18, no. 8, pp. 3843–3861, 2020.

[11] Y.-F. Zhang, J.-H. Zhang, and K. Demoha, "Further analysis on mechanical behaviors of blind-bolted T-stub connections to CFDST columns," *Structures*, vol. 48, pp. 1964–1976, 2023.

[12] P. Wang, Z. Wang, J. R. Pan, B. Li, and B. Wang, "Experimental study on seismic behavior of exterior composite beam-to-column joints with large size stiffened angles," *Steel and Composite Structures*, vol. 37, no. 1, pp. 15–26, 2020.

[13] Y. Luo and B. Wu, "Shear performance of steel plate-concrete joints connected with anchors and adhesive," *The Journal of Adhesion*, vol. 98, no. 7, pp. 889–914, 2022.

[14] D. Z. Hu, Z. Q. Yang, Q. C. Zhu, Z. P. Wu, and J. Zhao, "Experimental research on mechanic properties of prefabricated reinforced concrete beams with H-shaped steel joints," *Industrial Construction*, vol. 51, no. 6, pp. 59–66, 2021.

[15] M. Zeinizadeh Jeddi, N. H. Ramli Sulong, and M. M. Arabnejad Khanouki, "Seismic performance of a new through rib stiffener beam connection to concrete-filled steel tubular columns: an experimental study," *Engineering Structures*, vol. 131, pp. 477–491, 2017.

[16] M. Kurejková and F. Wald, "Design of haunches in structural steel joints," *Journal of Civil Engineering and Management*, vol. 23, no. 6, pp. 765–772, 2017.

[17] M. M. Nasery, M. Hüsem, F. Y. Okur, and A. C. Altunişik, "Damage effect on experimental modal parameters of haunch strengthened concrete-encased composite column–beam connections," *International Journal of Damage Mechanics*, vol. 29, no. 2, pp. 297–334, 2020.

[18] H. Saberi, A. Kheyroddin, and M. Gerami, "Welded haunches for seismic retrofitting of bolted T-stub connections and flexural strengthening of simple connections," *Engineering Structures*, vol. 129, pp. 31–43, 2016.

[19] H. Saberi, V. Saberi, A. Kheyroddin, and M. Gerami, "Seismic behavior of frames with bolted end plate connections rehabilitated by welded haunches under near-and far-fault earthquakes," *International Journal of Steel Structures*, vol. 19, no. 2, pp. 672–691, 2019.

[20] N. Tanaka, "Evaluation of maximum strength and optimum haunch length of steel beam-end with horizontal haunch," *Engineering Structures*, vol. 25, no. 2, pp. 229–239, 2003.

[21] C.-H. Lee, J.-H. Jung, M.-H. Oh, and E.-S. Koo, "Cyclic seismic testing of steel moment connections reinforced with welded straight haunch," *Engineering Structures*, vol. 25, no. 14, pp. 1743–1753, 2003.

[22] H. Van-Long, J. Jean-Pierre, and D. Jean-François, "Hammer head beam solution for beam-to-column joints in seismic resistant building frames," *Journal of Constructional Steel Research*, vol. 103, pp. 49–60, 2014.

[23] EN 1993-1-8, *Eurocode 3: Design of Steel Structures—Part 1–8: Design of joints*, European Committee for Standardization, Brussels, 2005.

[24] A. Lachal, J. M. Aribert, and G. Loho, "Static design and cyclic behavior of end-plate steel and composite joints strengthened by haunches," in *Proceedings of the Fourth International Conference on Advances in Steel Structures*, vol. 2, pp. 1353–1358, Elsevier Science Ltd., Shanghai, China, 2005.

[25] N. E. Shanmugam, Y. H. Ng, and J. Y. R. Liew, "Behaviour of composite haunched beam connection," *Engineering Structures*, vol. 24, no. 11, pp. 1451–1463, 2002.

[26] Q.-S. Yu, C.-M. Uang, and J. Gross, "Seismic rehabilitation design of steel moment connection with welded haunch," *Journal of Structural Engineering*, vol. 126, no. 1, pp. 69–78, 2000.

[27] Y. P. Chu, B. Jia, and L. L. Zhou, "Seismic behavior study on connections of multi-barrel tube-confined concrete column with steel beam," *Journal of Southwest University of Science and Technology*, vol. 24, pp. 7–12, 2009.

[28] J. L. Dong, Y. Wang, P. Zhuang, and Q. G. Li, "Experimental study on seismic behaviors of steel frames with haunch reinforced section connections," *China Civil Engineering Journal*, vol. 49, pp. 69–79, 2016.

[29] GB/T 228.1-2010, *Metallic Materials-Tensile Testing, Part 1: Method of Test at Room Temperature*, Standard Press of China, Beijing, 2010.

[30] Y.-F. Zhang and Z.-Q. Zhang, "Study on equivalent confinement coefficient of composite CFST column based on unified theory," *Mechanics of Advanced Materials and Structures*, vol. 23, no. 1, pp. 22–27, 2015.

[31] N. Abdel-Rahman and K. S. Sivakumaran, "Material properties models for analysis of cold-formed steel members," *Journal of Structural Engineering*, vol. 123, no. 9, pp. 1135–1143, 1997.

[32] V. Birtel and P. Mark, "Parameterised finite element modelling of RC beam shear failure," *Abaqus Users' Conference*, pp. 95–108, 2006.

[33] GB/T 50010-2010, *Code for Design of Concrete Structures*, China Architecture & Building Press, Beijing, 2010.

[34] L.-H. Han, G.-H. Yao, and Z. Tao, "Performance of concrete-filled thin-walled steel tubes under pure torsion," *Thin-Walled Structures*, vol. 45, no. 1, pp. 24–36, 2007.

[35] Y. F. Zhang, H. F. Bu, and S. X. Cao, "Seismic behavior investigations of the haunched joint with ribbed anchor webs in CFDST structures," *Research Square*, vol. 1, 2021, https://www.researchsquare.com/article/rs-699347/v1.